Contents lists available at: IJS

International Journal of Surgery

Journal homepage: ijsopen.org

Research Article

PRMT1 Regulates Glioma Stemness and Immunosuppression via Nitric Oxide Metabolism: Multi-Cohort Analysis and Experimental Validation

Kun Xue[1], Jiyong Cheng[2], Ya Gao[3,4], Caifeng Ma[3,5], Shuo Tang[3,4], Xinghan Tian[3], Yang Kong[3*] and Haiying Wang[6*]

[1]*Department of Neurosurgery, Yantaishan Hospital, Yantai, China*
[2]*Department of Neurosurgery, The Affiliated Yantai Yuhuangding Hospital of Qingdao University, Yantai, China*
[3]*Department of Critical Care Rehabilitation, The Affiliated Yantai Yuhuangding Hospital of Qingdao University, Yantai, China*
[4]*School of Clinical Medicine, Binzhou Medical University, Yantai, China*
[5]*School of Medicine, Qingdao University, Qingdao, China*
[6]*Department of Anesthesiology, The Affiliated Yantai Yuhuangding Hospital of Qingdao University, Yantai, China*

ARTICLE INFO

Keywords:
PRMT1
glioma
nitric oxide metabolism
cancer stem cells
immunosuppression
tumor microenvironment

ABSTRACT

Background: Glioblastoma represents the most common primary malignant brain tumor with dismal prognosis despite multimodal therapies. The immunosuppressive tumor microenvironment and cancer stem cell populations contribute to therapeutic resistance and recurrence. Nitric oxide (NO) metabolism has emerged as a critical regulator of tumor progression, yet its role in coordinating glioma stemness and immune evasion remains poorly understood.

Methods: We performed integrative multi-omics analysis using CGGA, TCGA, and Rembrandt datasets (n=1,500) to investigate NO metabolism patterns across glioma grades and molecular subtypes. Single-cell RNA sequencing data (SCP503, n=65,655 cells) characterized cellular heterogeneity and stemness features. *PRMT1* was identified through Cox regression and LASSO modeling as a key NO metabolism-associated prognostic gene. Functional validation used glioma cell lines and patient-derived glioma stem cells through knockdown/overexpression experiments, proliferation assays, invasion studies, and limiting dilution analysis. An orthotopic mouse model evaluated *PRMT1*'s role in tumor growth and stemness maintenance.

Results: NO metabolism activity progressively increased with glioma grade and correlated with poor survival (p<0.001). Single-cell analysis revealed significant positive correlation between NO metabolism and stemness scores (R=0.35, p<0.001). *PRMT1* expression was significantly elevated in high-grade gliomas and positively correlated with *NOS2* across multiple cohorts (R=0.26-0.46, p<0.001). Spatial transcriptomic analysis showed distinct expression patterns of *PRMT1* and *NOS2* in different glioma anatomical regions. Functional studies demonstrated that *PRMT1* knockdown significantly reduced cell proliferation (76% inhibition), colony formation (75% reduction), and stemness markers (CD133+ cells decreased from 11.74% to 3.11%). NO donor treatment rescued *PRMT1* knockdown effects, confirming the NO-dependent mechanism. In vivo experiments showed *PRMT1* silencing reduced tumor luminescence to 35% of controls (p<0.001) and decreased expression of stemness markers (*SOX2*) and immune checkpoint molecules (*PD-L1*).

Conclusion: *PRMT1* functions as a central hub linking NO metabolism to glioma stemness maintenance and immunosuppression. *PRMT1* regulates key stemness transcription factors (*OCT4*, *SOX2*) and immune checkpoint molecules (PD-L1) through NO-dependent mechanisms. These findings identify *PRMT1* as a potential therapeutic target that could simultaneously disrupt tumor stem cell populations and remodel the immunosuppressive microenvironment, providing a novel strategy for precision glioma therapy.

[*]*Corresponding author: Department of Anesthesiology, The Affiliated Yantai Yuhuangding Hospital of Qingdao University, No. 20, Yudong Road, Yantai City, Shandong Province, China; Tel: +86-0535-6691999; Fax: +860535826691999; E-mail: 418273519@qq.com* (Haiying Wang)
Department of Critical Care Rehabilitation, The Affiliated Yantai Yuhuangding Hospital of Qingdao University, No. 20, Yudong Road, Yantai City, Shandong Province, China; Tel: +8605356691999; Fax: +86-0535-826691999; E-mail: norwayky@163.com (Yang Kong)

10.60122/j.IJS.2025.40.14
Received 4 November, 2025; Accepted 12 December, 2025
Available online 10 January, 2026

1. Introduction

Glioma represents the most common primary malignant tumor of the central nervous system, comprising approximately 80% of adult brain cancers [1]. The profound heterogeneity and invasive nature of these tumors create an extremely poor prognosis for patients. Standard treatment protocols—surgery, radiotherapy, and chemotherapy with agents like temozolomide—have become established care, yet median survival for glioblastoma (GBM, WHO grade IV) remains a dismal 12-15 months [2]. Immunotherapy has achieved remarkable success across various solid tumors in recent years. However, GBM present a "cold" tumor microenvironment dominated by immunosuppressive cells, including regulatory T cells and tumor-associated macrophages [3, 4]. This hostile immune landscape severely limits the effectiveness of checkpoint inhibitors such as PD-1/*PD-L1* antibodies. Understanding how the GBM tumor microenvironment forms and identifying its key regulatory factors has become critical for improving immunotherapy outcomes [5].

Nitric oxide (NO) functions as a multifaceted signaling molecule, produced by the nitric oxide synthase (NOS) enzyme family: neuronal (NOS1), inducible (*NOS2*), and endothelial (NOS3) isoforms [6, 7]. The dual nature of NO metabolism in cancer biology has captured significant research attention [8]. Low concentrations promote blood vessel formation and tumor growth, while high concentrations trigger cell death and DNA damage. Current research shows that NO participates in inflammatory responses, vascular remodeling, and metabolic reprogramming within gliomas. The molecule potentially enhances tumor stemness maintenance and immune evasion through *NOS2* upregulation. For instance, NO activates HIF1A and STAT3 signaling pathways, promoting *PD-L1* expression and subsequently suppressing T-cell function [6, 9-11]. However, we lack a comprehensive understanding of how NO metabolism systematically controls the glioma immune microenvironment. The role of upstream regulatory molecules, particularly epigenetic modifying enzymes, in this process remains unclear.

Protein arginine methyltransferase 1 (*PRMT1*) serves as the predominant type I PRMT enzyme, catalyzing asymmetric dimethylation of arginine residues on histone and non-histone proteins [12, 13]. This enzyme participates in transcriptional regulation, signal transduction, and DNA repair mechanisms. Preliminary evidence indicates *PRMT1* overexpression in various cancers, correlating with poor patient outcomes [13, 14]. Yet its specific function within the glioma NO metabolic pathway remains undefined.

Our study investigates NO metabolism's role in glioma immune cell infiltration, molecular subtype distribution, and prognostic prediction through integrated bioinformatics analysis of multiple cohorts from CGGA, TCGA, and Rembrandt databases. We employed Cox regression and LASSO screening to identify key genes. Cell-level experiments, including knockdown/overexpression studies and proliferation/invasion assays, combined with *in vivo* mouse models, validated the function of our candidate gene *PRMT1*. We sought to understand its mechanisms in NO-dependent tumor stemness maintenance, chemoresistance, and immunosuppression. Our work culminates in a *PRMT1*-mediated regulatory model of the glioma microenvironment, providing a theoretical foundation for developing novel targeted therapies. These findings bridge metabolic reprogramming with immune microenvironment dynamics, advancing precision therapy for gliomas.

2. Methods

2. 1. Data Sources and Dataset Description

We obtained single-cell RNA sequencing (scRNA-seq) data from the Broad Institute Single Cell Portal public database (Study ID: SCP503; URL: Link 1) [15]. This dataset corresponds to Richards and colleagues' study published in Nature Cancer, encompassing 65,655 glioblastoma stem cells from tumor cultures of 28 patients. The data include normalized expression matrices, cell annotations, and dimensionality reduction coordinates.

Bulk RNA sequencing data for glioma came from the Chinese Glioma Genome Atlas (CGGA-glioma, n=326; URL: Link 2) [16] and The Cancer Genome Atlas (TCGA-glioma, n=699; URL: Link 3) [17]. We used these datasets for immune deconvolution and correlation analyses. Validation cohorts included Rembrandt glioma data (n=475) and micro-dissected sequencing data from the IVY Glioblastoma database (URL: Link 4) [18]. All RNA-seq data underwent standard normalization procedures. Gene expression levels are presented as fragments per kilobase of transcript per million mapped reads (FPKM).

Clinical information encompassed World Health Organization (WHO) grading, molecular subtypes (neural, proneural, classical, mesenchymal), isocitrate dehydrogenase (IDH) mutation status, 1p/19q co-deletion, and O6-methylguanine-DNA methyltransferase (MGMT) methylation status. We processed data using R software (v4.2.1), imputing missing values with median values and removing outliers through Z-score standardization.

2.2. Bioinformatics Analysis

2.2.1. Single-Cell RNA Sequencing Analysis

We conducted data processing in R (v4.2.1) using Seurat and Monocle3 packages [19, 20]. Quality control involved filtering cells with low gene detection (<200 genes), high mitochondrial gene content (>10%), or aberrant UMI counts (>2.5 standard deviations from the mean). Data normalization used log-transformation, while Harmony integration corrected batch effects. We performed dimensionality reduction using Principal Component Analysis (PCA) on the top 2,000 highly variable genes, followed by Uniform Manifold Approximation and Projection (UMAP) for visualization. Shared nearest neighbor (SNN)-based graph clustering identified cell subpopulations (resolution 0.8). Monocle3 enabled pseudotime trajectory inference for lineage differentiation, designating an early progenitor-like cluster as the root node. We calculated cancer stem cell (CSC) stemness scores based on established GSC marker gene sets (*SOX2*, *OLIG2*, *NES*, etc.). The Wilcoxon rank-sum test assessed differential gene expression, with Benjamini-

Hochberg adjustment for p-values. Significance thresholds were set at adjusted $p < 0.05$ and $|\log_2 \text{fold change (FC)}| \geq 1$.

2.2.2. Functional Enrichment and Metabolic Pathway Analysis

We performed functional annotation of differentially expressed genes (DEGs) using the clusterProfiler package, integrating Kyoto Encyclopedia of Genes and Genomes (KEGG) and Gene Ontology (GO) biological process databases. False discovery rate (FDR) < 0.05 served as the significance threshold [21, 22]. Metabolic pathway analysis drew from 73 predefined pathways within Wikipathways metabolism-related gene sets from the Molecular Signatures Database (MSigDB) [23]. Single-sample Gene Set Enrichment Analysis (ssGSEA) quantified pathway activity in each sample [24]. We calculated nitric oxide (NO) metabolism scores based on the "NITRIC_OXIDE_METABOLISM_IN_CYSTIC_FIBROSIS" gene set from MSigDB. Samples were divided into high-NO and low-NO groups based on median NO metabolism scores. The Mann-Whitney U test evaluated inter-group differences.

2.2.3. Immune Microenvironment Analysis

We deconvoluted immune cell infiltration using the CIBERSORT algorithm (Link 5) on CGGA glioma RNA-seq data [25]. The LM22 signature matrix estimated relative proportions of 22 immune cell types, validated through 1,000 permutations. The limma package handled differential expression analysis, with criteria set at $|\log_2 FC|>1$ and FDR<0.05. We assessed gene expression differences between high-NO and low-NO groups using appropriate statistical tests and visualized results with ggplot2. Spearman's rank correlation analysis constructed gene-immune cell association networks.

2.2.4. Prognostic Model Construction and Validation

Univariate Cox proportional hazards regression analysis used the survival package to screen genes associated with overall survival ($p<0.05$). We constructed prognostic models using LASSO (Least Absolute Shrinkage and Selection Operator) regression from the glmnet package, coupled with 10-fold cross-validation for optimal λ value selection [26]. Multivariate Cox regression validated independent prognostic factors. The VennDiagram package visualized gene intersection relationships, while the Kruskal-Wallis test compared molecular subtypes. We generated Kaplan-Meier survival curves through survminer and assessed inter-group survival differences using the log-rank test.

2.3. Clinical Samples and Cell Culture

We collected glioblastoma tissue samples (n=30, including normal brain tissue and WHO grade II-IV gliomas) from patients at our institution, with Institutional Review Board approval (Approval No.: YTM-2025193). All participants provided written informed consent. Samples underwent immediate fixation in 10% formalin after surgical resection for immunohistochemical (IHC) staining.

Human glioma cell line culture included U251, U87MG, and A172 cell lines (ATCC source) along with primary glioma cells GBM#P3 for in vitro functional validation. We cultured cells in DMEM/F12 medium (Gibco) supplemented with 10% fetal bovine serum (FBS; Gibco) and 1% penicillin-streptomycin (Gibco) at 37°C with 5% CO_2. Stem cell experiments used GBM#P3 cells maintained in serum-free Neurobasal Medium (Gibco) with epidermal growth factor (EGF; 20 ng/mL) and basic fibroblast growth factor (bFGF; 20 ng/mL).

For murine studies, GL261 cells were cultured in DMEM high-glucose medium (Gibco) with 10% FBS, 1% penicillin-streptomycin, 1% L-glutamine (Gibco), and 1% non-essential amino acids (Gibco) at 37°C with 5% CO_2. We established a stable bioluminescence imaging model by transducing GL261 cells with lentivirus expressing luciferase (GL261-Luc). Puromycin selection (2 μg/mL) isolated positive clones after transduction. Regular luciferase activity assays verified reporter gene expression stability.

Transfection procedures used Lipofectamine 2000 (Invitrogen) for small interfering RNA (si-*PRMT1*, si-*SOX2*, si-HIF1A; GenePharma synthesis) or pcDNA3.1-*PRMT1* plasmid overexpression. Western blot confirmed transfection efficiency. We applied the NO donor S-nitroso-N-acetylpenicillamine (SNAP; Sigma-Aldrich) at 0-150 μM concentrations for 24 hours.

Small interfering sequences were: si-*PRMT1*-1: 5'-CGUCAAAGCCAACAAGUUA-3'; si-*PRMT1*-2: 5'-GUGAGAAGCCCAACGCUGA-3'; si-*SOX2*: 5'-CCCGCAUGUACAACAUGAUUU-3'; si-HIF1A: 5'-GAGCUCCCAUCUUGAUAAATT-3'.

2.4. Molecular Biological Detection

2.4.1. Western Blot Analysis

We lysed cells using RIPA buffer (Beyotime) and determined protein concentrations with a BCA kit (Thermo Fisher). Samples (20 μg) underwent SDS-PAGE separation before transfer to PVDF membranes (Millipore). Primary antibodies included anti-*PRMT1* (Abcam, ab190892, 1:1000), anti-*iNOS* (Proteintech, 22226-1-AP, 1:1000), anti-*SOX2* (Proteintech, 66411-1-Ig, 1:1000), anti-*OCT4* (Abcam, ab184665, 1:1000), anti-*PD-L1* (Abcam, ab213524, 1:1000), and anti-β-Tubulin (Abcam, ab178945, 1:5000). HRP-conjugated goat anti-rabbit IgG (Beyotime, A0208 and A0216,1:5000) served as secondary antibodies. ECL reagent (Millipore) enabled signal detection, with ImageJ software for quantification.

2.4.2. Immunohistochemical Staining

Tissue sections (4μm) underwent deparaffinization, rehydration, and antigen retrieval. Primary antibodies included anti-*PRMT1* (Abcam, 1:200), anti-*SOX2* (Proteintech, 1:100), anti-*PD-L1* (Abcam, 1:100), and anti-*iNOS* (Proteintech, 1:100), with HRP-conjugated secondary antibodies (Beyotime). DAB provided chromogenic development, followed by hematoxylin counterstaining.

2.5. Cell Function Experiments

2.5.1. Proliferation and Colony Formation Assays

For EdU proliferation assays, we seeded GBM cells (U251 and A172) in 24-well plates (2×10^4/well). After transfection, 10 μM EdU (Beyotime) was added for 2-hour incubation. We fixed cells, applied Apollo staining solution, and counterstained with DAPI. Fluorescence microscopy (Olympus) enabled observation, with ImageJ quantifying positive cells. Plate colony formation assays involved seeding GBM cells (U251 and A172) in 6-well plates (500/well). After 14 days of culture, crystal violet stained colonies for ImageJ counting.

Stem cell sphere formation assays used GBM#P3 cells cultured in suspension in low-adhesion 6-well plates (1,000/well) for 7 days. We observed sphere morphology and size microscopically. Extreme limiting dilution analysis (ELDA) in vitro involved seeding treated GBM#P3 cells at decreasing densities (1, 5, 10, 25, 50 cells/well) in 96-well ultra-low attachment plates with 8 replicate wells per concentration [27]. After 10 days of culture, we counted formed stem cell spheres (diameter >50 μm) under microscopy. The online ELDA analysis tool (Link 6) calculated tumor-initiating cell frequency.

2.5.2. Invasion and Stemness Assays

Transwell invasion assays employed Matrigel-pre-coated inserts (Corning). We seeded 5×10^4 cells in upper chambers with culture medium containing 10% FBS in lower chambers. After 24 hours of invasion, cells were fixed, stained, and counted microscopically. Flow cytometry analysis examined GBM#P3 cells after various treatments, using single staining with *CD133* and *PD-L1* antibodies to analyze positive cell proportions.

2.6. Animal Experiments

We used male C57BL/6 mice (6-8 weeks old; Vital River Laboratory) to establish orthotopic glioma models. GL261-Luc cells (stably expressing luciferase; 2×10^5) underwent stereotactic injection into the right cerebral hemisphere (coordinates: 2 mm right of bregma, 2 mm posterior, 3 mm deep). Experimental groups included sh-Control and sh-*PRMT1* groups (n=6 mice per group). We monitored tumor growth through bioluminescence imaging (BLI) using the IVIS system (PerkinElmer), quantifying photon flux after D-luciferin injection (150 mg/kg) to assess tumor burden. Kaplan-Meier methodology analyzed survival data. Hematoxylin-eosin (H&E) staining provided histological evaluation. The Institutional Animal Care and Use Committee approved all animal experiments.

2.7. Statistical Analysis

Data are presented as mean ± standard deviation. We performed group comparisons using Student's t-test or one-way analysis of variance (ANOVA), with Bonferroni correction for multiple comparisons. Spearman's rank correlation method assessed correlations. The log-rank test evaluated survival differences. All analyses used GraphPad Prism (v9.0) and R software, with $p < 0.05$ considered statistically significant.

3. Results

3.1. ssGSEA Analysis of Metabolic Pathways and Their Association with Tumor Stemness across Glioma Pathological Grades

We performed ssGSEA on the CGGA-glioma dataset, calculating pathway scores for each sample and creating hierarchical clustering heatmaps (Figure 1A). Metabolic pathway scores showed consistent patterns across different pathological grades of glioma samples. Blue-dominated clusters indicated suppressed pathways, while red clusters represented activated ones. Activated pathways included AMINO_ACID_METABOLISM_IN_TRIPLE_NEGATIVE_BREAST_CANCER_CELLS, SERINE_METABOLISM, ARSENIC_METABOLISM_AND_REACTIVE_OXYGEN_SPECIES_GENERATION, PENTOSE_PHOSPHATE_METABOLISM, NITRIC_OXIDE_METABOLISM_IN_CYSTIC_FIBROSIS, METABOLISM_OF_SPHINGOLIPIDS_IN_ER_AND_GOLGI_APPARATUS, PATHWAYS_OF_NUCLEIC_ACID_METABOLISM_AND_INNATE_IMMUNE_SENSING, and IRON_METABOLISM_DISORDERS. These activated pathways suggest that glioma proliferation involves enhanced immunosuppression and oxidative stress, accompanied by increased amino acid and nucleic acid metabolism. Suppressed pathways included ARYLAMINE_METABOLISM, TAMOXIFEN_METABOLISM, NICOTINE_METABOLISM_IN_LIVER_CELLS, CODEINE_AND_MORPHINE_METABOLISM, and EICOSANOID_METABOLISM_VIA_CYCLOOXYGENASES_COX. These pathways primarily involve metabolism of exogenous substances (drugs, toxins) and inflammatory mediators, potentially reflecting glioma metabolic reprogramming and reduced clearance of metabolic byproducts.

We examined several pathways in detail. Nucleic acid metabolism and immunosuppression pathway ssGSEA scores increased with higher glioma pathological grades, indicating that accelerated pathological proliferation enhances nucleic acid metabolism while promoting severe immunosuppression (Figure 1B). Iron metabolism showed similar trends, with increasing dysregulation at higher pathological grades (Figure 1D). Nitric oxide metabolism pathway scores rose from a median of approximately 0.21 (WHO II) to 0.22 (WHO IV), demonstrating active nitric oxide metabolism in glioma samples, particularly pronounced in high-grade tumors (Figure 1C).

Phosphatidyl*iNOS*itol metabolism ssGSEA scores declined from median values of approximately 0.238 (WHO II) to 0.227 (WHO III), further decreasing to 0.205 (WHO IV), with significant differences between pathological grades (Kruskal-Wallis test, p <2.2e-16, Figure 1E). The METABOLISM_OF_SPHINGOLIPIDS_IN_ER_AND_GOLGI pathway also showed declining scores from median values of about 0.255 (WHO II) to 0.245 (WHO III) and 0.231 (WHO IV), with significant differences (Kruskal-Wallis test, p=1.1e-08, Figure 1F).

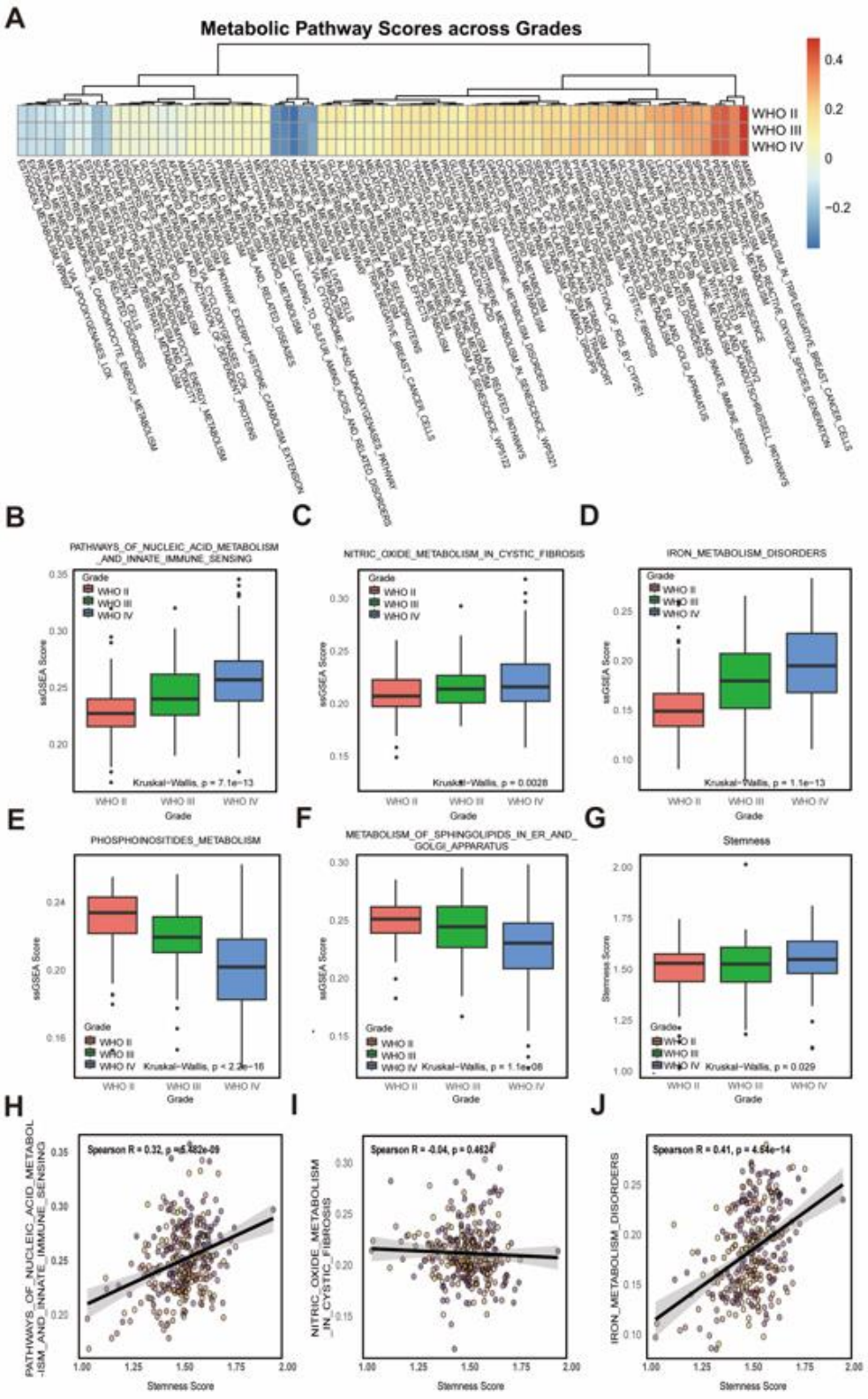

Fig. 1. Metabolic pathway differences across glioma pathological grades and stemness associations.

A) Hierarchical clustering heatmap of ssGSEA scores for 73 metabolic pathways in CGGA dataset showing suppressed pathways (blue) and activated pathways (red). **B)** Box plot analysis demonstrating nucleic acid metabolism and immunosuppression pathway scores increasing with WHO grades. **C)**

Distribution patterns of nitric oxide metabolism pathway scores across different WHO grades. **D)** Iron metabolism disorder pathway changes with tumor grading progression. **E)** Phosphatidylinositol metabolism score differences between grades (Kruskal-Wallis test, $p < 2.2e-16$). **F)** ER and Golgi sphingolipid metabolism pathway grade correlations ($p = 1.1e-08$). **G)** Tumor stemness score distribution across WHO grades II-IV ($p = 0.029$). **H)** Correlation scatter plot between nucleic acid metabolism pathway and tumor stemness (R = 0.32, $p = 5.48e-09$). **I)** Correlation analysis between nitric oxide metabolism and stemness scores (R = -0.04, $p = 0.4624$). **J)** Positive correlation between iron metabolism disorders and tumor stemness (R = 0.41, $p = 4.64e-14$).

Tumor stemness score analysis revealed significant differences among WHO grades: WHO II glioma samples had median stemness scores of approximately 1.52, WHO III samples about 1.55, and WHO IV glioblastoma samples about 1.59 (Kruskal-Wallis test, p=0.029, Figure 1G). We examined associations between specific metabolic pathways and tumor stemness. Spearman correlation analysis showed positive correlations between nucleic acid metabolism and innate immune sensing pathways scores and tumor stemness scores (Figure 1H, R = 0.32, p =5.48e-09). Iron metabolism disorders scores also showed significant positive correlations with tumor stemness (Figure 1J, R = 0.41, p =4.64e-14). However, nitric oxide metabolism scores showed no significant correlation with tumor stemness (Figure 1I, R = -0.04, p =0.4624).

The bulk sequencing data may have limited sensitivity for detecting subtle associations between overall nitric oxide metabolism activity and tumor stemness due to sample heterogeneity. We therefore analyzed single-cell sequencing data from glioma samples to reveal more precise cell-specific regulatory patterns.

3.2. Single-Cell Transcriptome Sequencing Reveals Glioma Cell Heterogeneity, Stemness Features, and Metabolic Regulation

Our analysis of the SCP503 single-cell sequencing dataset complemented bulk RNA-seq observations regarding glioma metabolic activation patterns (such as overall nitric oxide metabolism activity) while revealing cellular-level heterogeneity. Unsupervised clustering combined with UMAP analysis identified 27 distinct cell populations (Figure 2A) with significant differences in marker genes and functional states (Figure 2B). Pseudotime trajectory reconstruction using Monocle3 (Figure 2C) showed that these cells distributed primarily along a continuous path, initiating from Cluster 22 toward terminal differentiation at Cluster 10. Cluster 22 occupied the beginning of the developmental trajectory (low pseudotime value, undifferentiated state), while Cluster 10 resided at the terminal end (high pseudotime value, differentiated state) (Figure 2E).

Cell stemness scoring revealed significant differences among subpopulations, with Cluster 22 exhibiting significantly higher stemness scores than Cluster 10 (Wilcoxon test, p <0.001, Figure 2D). This aligned with Cluster 22's low pseudotime values, indicating its high-stemness, undifferentiated state. Comparing differentially expressed genes between clusters (Figure 2F), neurodevelopmental and proliferation-related genes highly expressed in Cluster 22 included *C1orf61*, *OLIG2*, *ASCL1*, *OLIG1*, *GRIA2*, *BCAN*, *DLL3*, *ELAVL3*, *XIST*, and *C2orf80*. In contrast, highly expressed genes in Cluster 10 included *CDKN2A*, *KRT18*, *HOXB-AS3*, *CXCL6*, *CXCL8*, *RNF212B*, *MMP1*, *COL1A1*, *CRHBP*, and *CDKN2B*, associated with extracellular matrix organization, astrocytic differentiation, and inflammatory signaling.

KEGG enrichment analysis of highly expressed differentially expressed genes (Figure 2G) primarily enriched neurodegenerative disease pathways (Alzheimer's disease, Huntington's disease) and cell cycle regulation pathways (FDR <0.05). GO cellular function enrichment analysis (Figure 2H) showed enrichment in proliferation-related terms including chromosome segregation, DNA replication, and sister chromatid cohesion (FDR <0.05). Metabolic pathway correlation analysis (Figure 2I) revealed that at the single-cell level, glioma cell stemness scores significantly positively correlated with nitric oxide metabolism scores (Spearman R = 0.35, p = 1.2e-05) and tryptophan metabolism scores (Spearman R =0.28, p =4.5e-04). These results highlight nitric oxide metabolism's critical role in glioma progression, potentially serving as a core metabolic axis for maintaining tumor stemness and promoting heterogeneity, thus offering new therapeutic targets.

3.3. Differential Analysis of Immune Microenvironment Features in NO Metabolism Groups

To explore NO metabolism mechanisms in gliomas, we analyzed differential immune microenvironment characteristics based on NO metabolism grouping. Distribution patterns of 22 immune cell types in the CGGA glioma cohort, shown in immune infiltration stacked bar charts (Figure 3A), revealed significant inter-sample immune heterogeneity. Macrophages (M0, M1, M2 subtypes), neutrophils, monocytes, and memory CD4+ T cells showed relatively high infiltration levels in most samples, while B cells, NK cells, and some T cell subsets exhibited lower infiltration. This immune heterogeneity reflects glioma microenvironment complexity and individual variability, providing crucial insights for personalized immunotherapy strategies.

NO metabolism score-based grouping revealed significant immune cell composition differences. Resting memory CD4+ T cells were significantly enriched in the low NO metabolism group ($p < 0.05$, Figure 3B), suggesting NO metabolism might inhibit memory T cell maintenance through cytotoxic effects or metabolic interference. Conversely, regulatory T cells (Tregs) accumulated significantly in the high NO metabolism group ($p < 0.05$, Figure 3C), possibly due to NO directly promoting Treg differentiation and expansion or creating favorable microenvironmental conditions. Notably, M0 macrophages were also significantly enriched in the high NO metabolism group ($p <$ 0.05, Figure 3D), indicating NO metabolic products might influence macrophage polarization programs, hindering M1 differentiation or promoting M2 conversion, thereby establishing an immunosuppressive microenvironment.

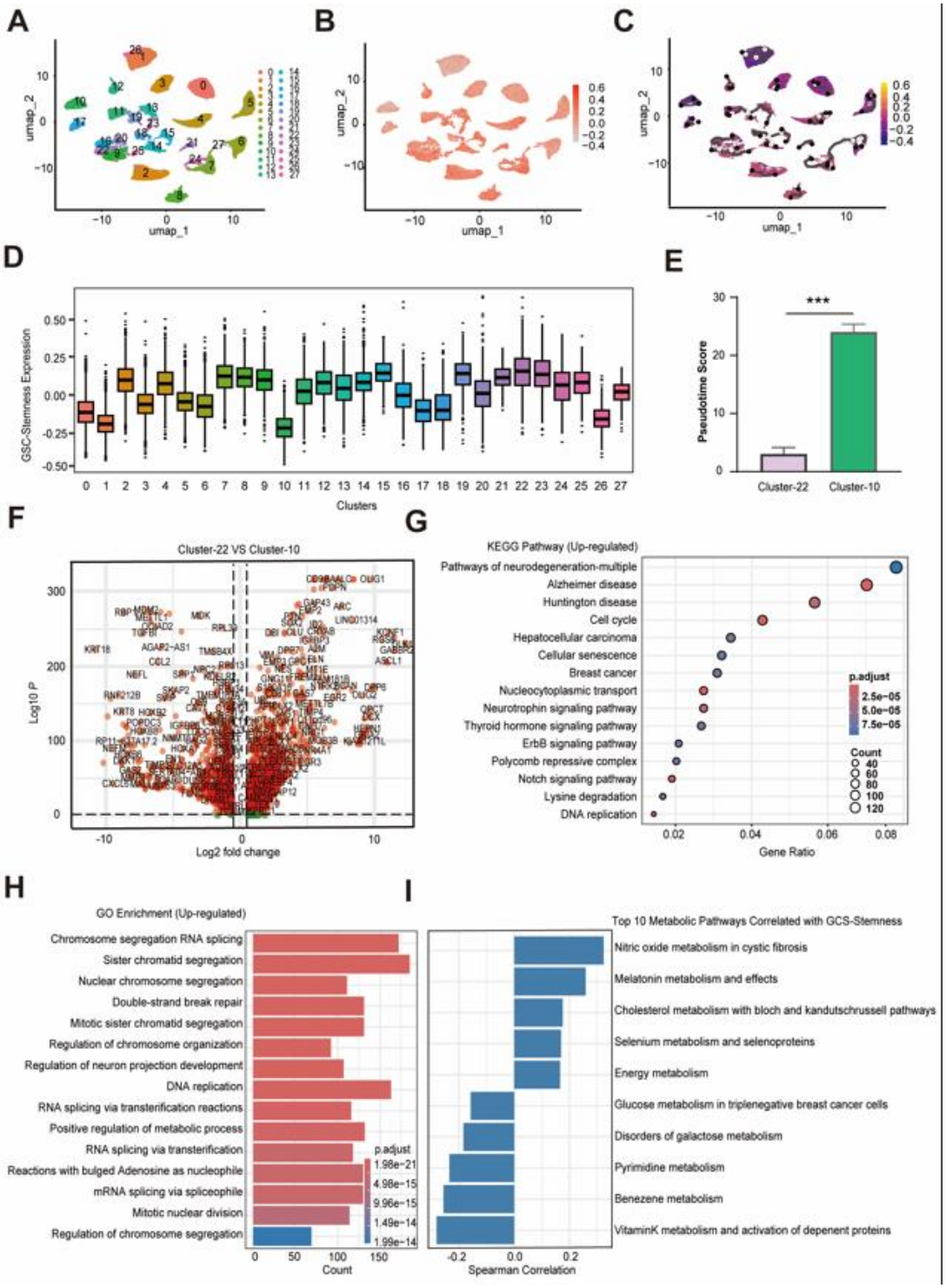

Fig. 2. Single-cell sequencing reveals glioma heterogeneity and stemness features.

A) UMAP visualization of 27 distinct cell clusters. **B)** Heatmap of marker gene expression across different cell populations. **C)** Monocle3-constructed pseudotime trajectory showing cell differentiation paths. **D)** Comparison of stemness scores between Cluster 22 and Cluster 10 (Wilcoxon test, $p < 0.001$). **E)** Pseudotime values confirming cell differentiation states. **F)** Volcano plot of differentially expressed genes between high and low stemness populations. **G)** KEGG pathway enrichment analysis of upregulated genes (FDR < 0.05). **H)** GO biological process enrichment results highlighting proliferation-related functions. **I)** Single-cell level correlations between stemness scores and metabolic pathways, with NO metabolism showing significant positive correlation ($R = 0.35$, $p = 1.2e-05$) and tryptophan metabolism displaying similar trends ($R = 0.28$, $p = 4.5e-04$).

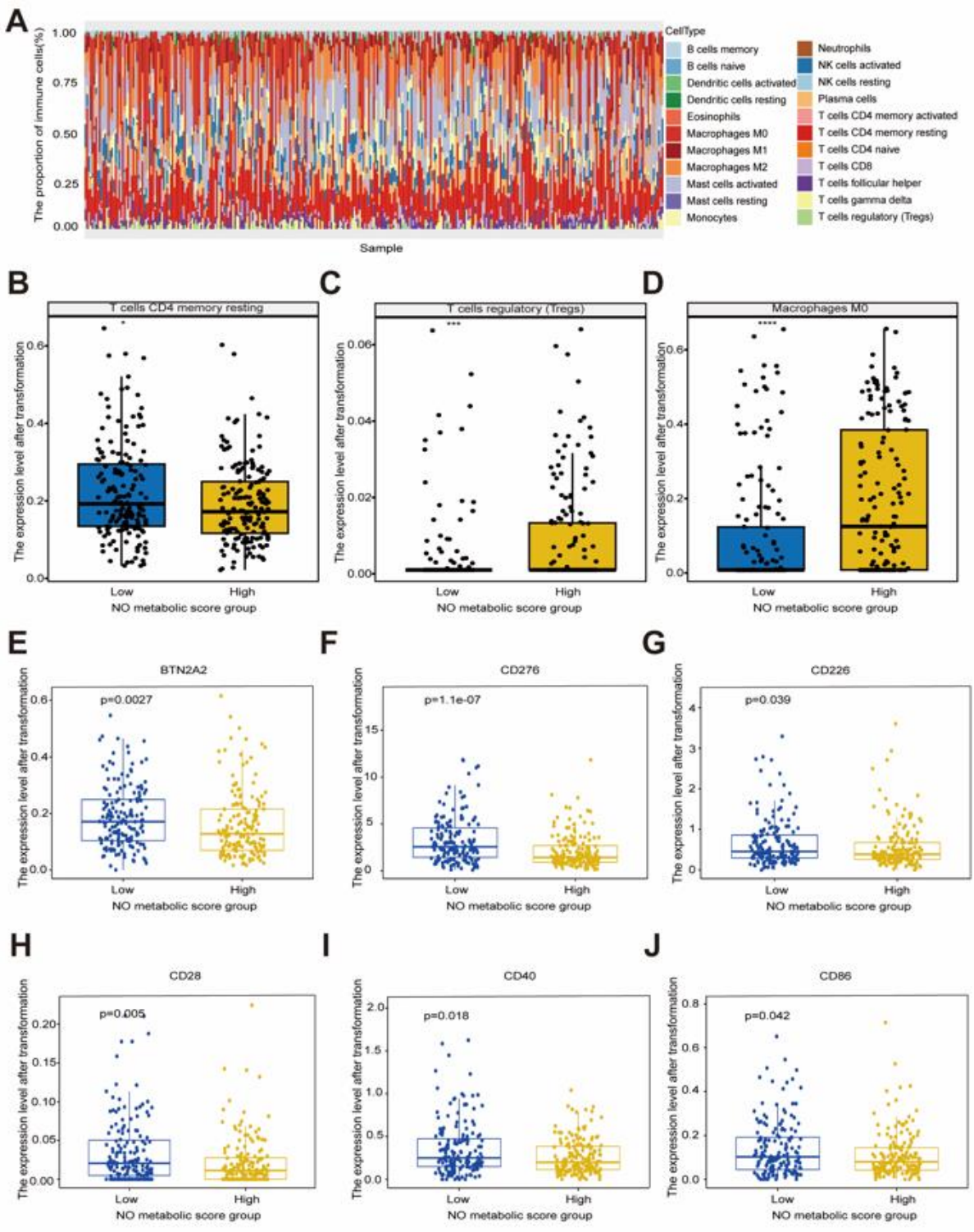

Fig. 3. Immune microenvironment differences between NO metabolism groups.

A) Stacked bar chart showing relative proportions of 22 immune cell types in CGGA cohort. **B)** Enrichment of resting memory CD4+ T cells in low NO metabolism group ($p < 0.05$). **C)** Accumulation of regulatory T cells in high NO metabolism group ($p < 0.05$). **D)** Association of M0 macrophages with high NO metabolism group ($p < 0.05$). **E-J)** Expression differences of immune regulatory molecules between NO metabolism groups, demonstrating systematic downregulation of *BTN2A2* (p= 0.0027), *CD276/B7-H3* (p= 1.1e-07), *CD226* (p= 0.039), *CD28* (p<0.005), *CD40* (p= 0.018), and *CD86* (p= 0.042).

Expression analysis of immunoregulatory molecules confirmed NO metabolism's immunosuppressive role. Key immune molecules showed systematic downregulation trends in the high NO metabolism group (Figures 3E-3J), including immune checkpoint molecules like *BTN2A2* (p = 0.0027) and *CD276/B7-H3* (p = 1.1e-07), along with T cell co-stimulatory molecules like *CD226* (p = 0.039), *CD28* (p < 0.005), *CD40* (p = 0.018), and *CD86* (p = 0.042). This systematic suppression forms a complete immunosuppressive profile: downregulated CD28 expression affects T cell activation thresholds, reduced *CD40* and *CD86* diminish antigen presentation efficiency, and *CD226* inhibition weakens cytotoxic effects. These findings reveal NO metabolism's critical role in glioma immune evasion, suggesting NO metabolism scores could serve as biomarkers for predicting immunotherapy response, providing theoretical foundations and potential therapeutic targets for precision glioma immunotherapy. Based on these immune microenvironment analysis results, we conducted prognostic value analysis of NO metabolism-related genes in gliomas to evaluate their clinical application potential.

3.4. Prognostic Value Analysis of NO Metabolism-Related Genes in Glioma

Analysis from two independent cohorts, CGGA and TCGA, demonstrated strong correlations between NO metabolism scores and key molecular features of glioma. In the CGGA cohort, NO metabolism score distributions across four molecular subtypes (Neural, Proneural, Classical, Mesenchymal) showed significant differences (Figure 4A), with classical gliomas exhibiting the highest NO metabolic activity and mesenchymal subtypes relatively lower. Furthermore, high-grade gliomas (WHO grade III-IV) displayed significantly higher NO metabolic activity than low-grade tumors (Figure 4B), indicating positive correlations between NO metabolism and tumor malignancy. Survival analysis confirmed the clinical significance of NO metabolism scores, as high-group patients had significantly shorter overall survival (p < 0.001, Figure 4C).

TCGA cohort validation analysis showed consistent trends with the CGGA cohort. Molecular subtype distribution patterns were largely similar (Figure 4D), further supporting NO metabolism score stability and reproducibility. Methylation status analysis revealed non-methylated groups had significantly higher NO metabolism scores than methylated groups (p < 0.05, Figure 4E), suggesting potential links between NO metabolism and DNA methylation regulatory mechanisms. Notably, genomic instability analysis indicated significantly higher chromosomal aneuploidy percentages in high NO metabolism groups (p < 0.001, Figure 4F), implying NO metabolism might contribute to maintaining genomic instability and promoting tumor progression.

Through systematic survival analysis, we identified key genes with independent prognostic value. Univariate Cox regression analysis in the TCGA glioma cohort screened multiple significant prognosis-related genes (Figure 4G), including *TMEM8A*, *GNL2*, *LYPLA2*, *SNRNP40*, and *WDR77*, with high expression correlating with poor prognosis (HR > 1, p < 0.05). TCGA low-grade glioma subgroup analysis revealed specific prognostic gene sets for this subgroup (Figure 4H), including *LRRC42*, *SNRNP40*, and *WDR77*. These genes involve crucial cellular processes such as transcriptional regulation, protein metabolism, and DNA repair.

We employed LASSO regression methodology for feature selection and model optimization (Figure 4I). Through ten-fold cross-validation for optimal regularization parameter λ selection, LASSO analysis identified core gene sets from numerous prognosis-related genes, including *ADPRHL2*, *HDAC1*, *WDR77*, *ALDH5A1*, *WASF3*, *NDRG2*, *TSPAN7*, *ZDHHC18*, *CAMK2G*, *RTN1*, *PSMB2*, and *TTF2*. These genes demonstrated solid statistical performance in prognostic model construction.

Given this study's focus on NO metabolic pathway regulatory mechanisms, we adopted a biologically guided screening strategy. This involved intersecting single-gene Cox analysis results from four cohorts (CGGA-GBM, CGGA-Glioma, TCGA-Glioma, and TCGA-LGG) with NITRIC_OXIDE_METABOLISM_IN_CYSTIC_FIBROSIS metabolic pathway genes. Venn diagram analysis showed extensive overlap of differentially expressed genes across the four datasets. Intersection with the nitric oxide metabolism pathway ultimately identified one common gene—*PRMT1* (Figure 4J). As a key epigenetic regulatory enzyme, *PRMT1* is overexpressed in various cancers and promotes tumor growth. In gliomas, it may regulate gene transcription through arginine methylation modifications, participating in NO metabolic pathway regulation and providing new potential therapeutic targets for glioma treatment.

3.5. *PRMT1* Expression Characteristics and NO Metabolism Associations in Different Glioma Cohorts

Analysis of three independent glioma datasets revealed that *PRMT1* consistently showed significant upregulation with increasing pathological grades (Figures 5A-5C). In the CGGA cohort, *PRMT1* expression in WHO grade IV glioblastoma was significantly higher than in grade II and III gliomas (p<0.001). TCGA and Rembrandt cohort analyses confirmed these trends, indicating close associations between high *PRMT1* expression and glioma malignancy, consistent with its oncogenic biological properties.

Molecular subtype analysis revealed significant expression pattern differences across the three datasets (Figures 5D-5F). The CGGA cohort (Figure 5D) showed highest *PRMT1* expression in the Proneural subtype and lowest in the Classical subtype (p < 0.001). However, the TCGA cohort (Fig. 5E) presented inverse patterns, with highest *PRMT1* expression in the classical subtype and relatively lower in the Proneural subtype. The Rembrandt cohort (Figure 5F) exhibited relatively smaller expression differences among subtypes. Such inter-cohort variability might reflect population genetic background heterogeneity. For instance, *IDH* mutation frequency is generally lower in Asian populations compared to Western populations, potentially affecting *PRMT1* expression patterns indirectly. This cohort-specific difference highlights biomarker universality challenges: as an epigenetic regulatory enzyme, *PRMT1*'s function may be context-dependent, requiring attention to its functional state within specific molecular backgrounds when developing targeted therapeutic strategies.

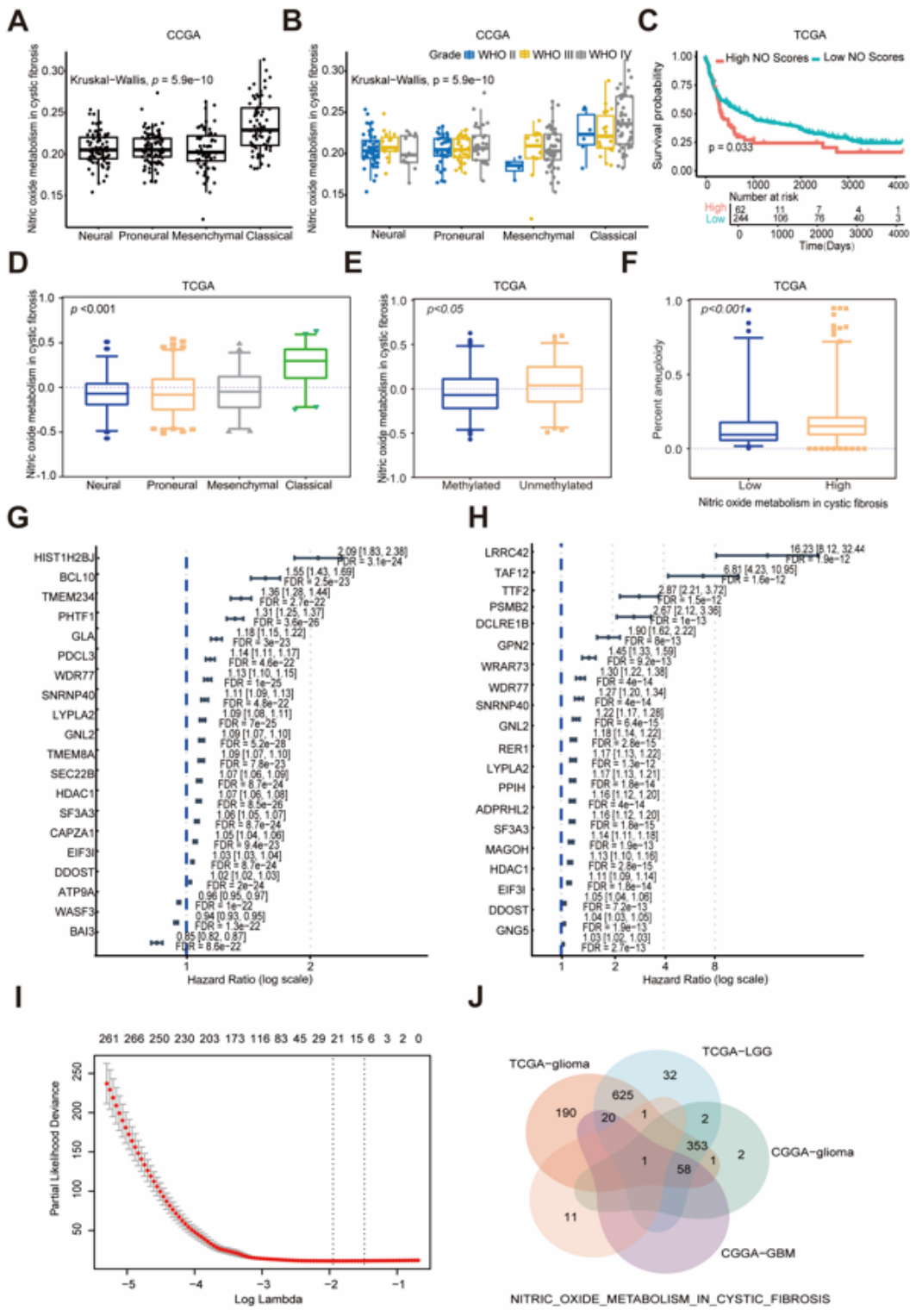

Fig. 4. Prognostic significance of NO metabolism-related genes.

A) Distribution of NO metabolism scores across molecular subtypes in CGGA cohort. **B)** High-grade gliomas showing significantly higher NO metabolic activity than low-grade tumors. **C)** Kaplan-Meier survival curves based on NO metabolism scores (p<0.001, log-rank test). **D)** TCGA cohort validation of molecular subtype distribution patterns. **E)** Relationship between methylation status and NO metabolism scores (p < 0.05). **F)** Association of chromosomal aneuploidy with high NO metabolism groups (p<0.001). **G)** Forest plot of univariate Cox regression analysis in TCGA glioma cohort. **H)** Subtype-specific

prognostic gene analysis in low-grade glioma subgroup. **I)** LASSO regression λ selection and coefficient path plot. **J)** Venn diagram identifying *PRMT1* as common gene through four-cohort intersection analysis.

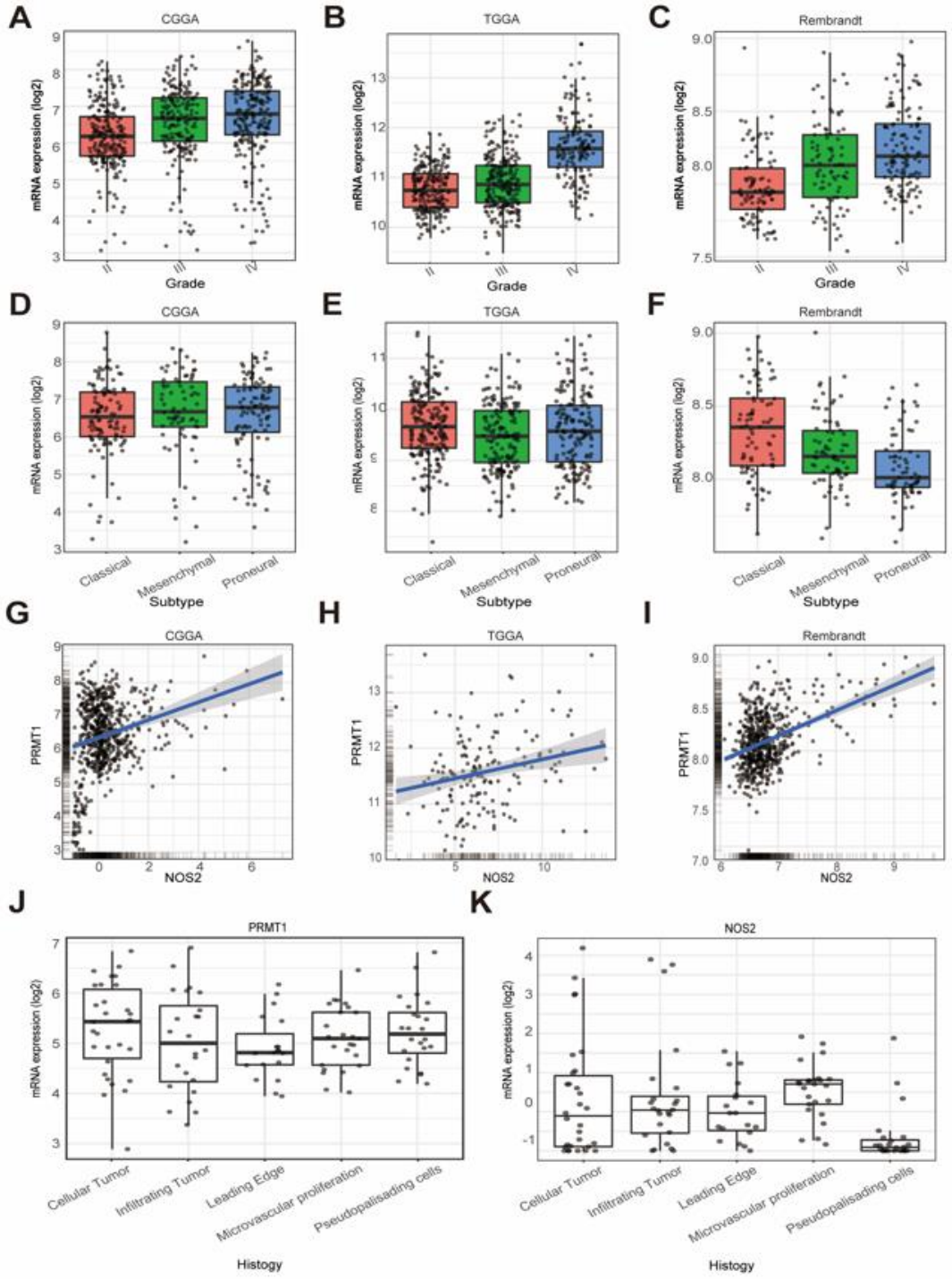

Fig. 5. *PRMT1* expression characteristics across different glioma cohorts.

A-C) *PRMT1* expression upregulation trends with pathological grades in CGGA, TCGA, and Rembrandt datasets ($p < 0.001$). **D-F)** *PRMT1* expression pattern differences among molecular subtypes in three datasets. **G-I)** Positive correlations between *PRMT1* and *NOS2* across cohorts with correlation coefficients of CGGA: r = 0.26, TCGA: r = 0.30, Rembrandt: r = 0.46 (all $p < 0.001$). **J-K)** Spatial expression patterns of *PRMT1* and *NOS2* in microdissected regions from IVY database.

PRMT1 and *NOS2* exhibited significant positive correlations across all three datasets (Figures 5G-5I), with correlation coefficients of r = 0.26 ($p < 0.001$) in the CGGA cohort, r = 0.30 ($p < 0.001$) in the TCGA cohort, and r = 0.46 ($p < 0.001$) in the Rembrandt cohort. While these correlation coefficients represent moderate effect sizes, their consistency across cohorts supports the hypothesis that *PRMT1* participates in NO metabolism regulation, providing crucial leads for functional validation studies.

Microdissected sequencing analysis based on the IVY Glioblastoma Atlas Project (IVY-GAP) database (Figures 5J-5K) revealed significant spatial heterogeneity of *PRMT1* and *NOS2* across different glioma histological regions. These regions included cellular tumor, infiltrating tumor, leading edge, microvascular proliferation, and pseudopalisading cells around necrosis. The two genes showed distinct expression patterns: *PRMT1* expression was highest in cellular tumor regions and lowest in leading edge regions, while *NOS2* was most highly expressed in microvascular proliferation regions and lowest in pseudopalisading cells around necrosis. This spatial distribution difference suggests *PRMT1* primarily participates in regulating core glioma cell growth and proliferation, while *NOS2* is more associated with tumor angiogenesis and microenvironmental adaptation, potentially promoting inflammatory responses and invasive behaviors. Further validation studies could confirm these associations and explore their potential mechanisms in glioma progression.

3.6. *PRMT1* Expression Validation and Functional Studies in Glioma

Immunohistochemical (IHC) staining results validated *PRMT1* protein expression patterns in glioma tissues, showing high consistency with previous transcriptomic data (mRNA level). Figure 6A displays staining results for normal brain tissue and WHO grade II, III, and IV gliomas, with *PRMT1* in the upper row and *iNOS* in the lower row. Normal brain tissue showed weak *PRMT1* signals, but as glioma malignancy increased, *PRMT1*-positive cell proportions rose significantly (approximately 25-30% in grade II, 50-60% in grade III, and over 80% in grade IV). Staining intensity (nuclear, cytoplasmic, and granular distribution) increased from mild to strong diffuse expression, peaking particularly in grade IV glioblastoma (GBM), consistent with high mRNA expression trends. *iNOS* staining exhibited similar increasing patterns, with positive cell proportions rising from < 10% in normal tissue to 60-70% in grade IV, and staining intensity increasing from weak to significant levels. This supports *PRMT1*'s correlation in tumor progression and suggests potential synergistic action through inflammatory and epigenetic axes. Quantitative analysis confirmed this trend, showing approximately 6-8-fold increases in staining intensity and positive ratios with escalating grade (Figures 6B & 6C).

Western blot analysis (Figure 6D) independently verified *PRMT1* protein levels in various glioma cell lines (U251, U87MG, A172, and primary GBM#3). Supplementary Figure S-F1A densitometric quantification showed relative expression values (normalized to β-tubulin) increased from approximately 0.98±0.15 in U251 to 1.2±0.2 in GBM#3, a difference of about 1.5-2 fold. Functional validation experiments using knockdown and overexpression strategies reinforced *PRMT1*'s biological role. Figure 6E demonstrates that si*PRMT1*-1 and si*PRMT1*-2 knockdown significantly reduced *PRMT1* protein levels in U251 cells (vs. siControl), with S-F1B densitometric quantification showing relative expression decreasing to 52±5% and 22±3% of control after knockdown. Figure 6-F shows enhanced *PRMT1* bands in A172 cells with OE *PRMT1* overexpression (vs. OE Vector), with S-F1C densitometric quantification showing expression increasing to 2.1±0.6 times control levels.

EdU proliferation assay results highlighted *PRMT1*'s critical role in regulating glioma cell proliferation. Figure 6G shows significant reduction in EdU-positive U251 cells after *PRMT1* knockdown, with S-F1D quantitative results showing proportions decreasing from 38±4% in controls to 10±3% (approximately 76% inhibition rate). Conversely, Figure 6H shows notable increases in EdU-positive A172 cells upon *PRMT1* overexpression, with S-F1E quantitative results showing proportions rising from 13±3% to 34±5%. Plate colony formation assays confirmed these results: Figure 6I shows significant decreases in U251 cell colony formation ability after *PRMT1* knockdown, with S-F1F quantitative results showing colony numbers reducing from 135±12 in controls to 35±8 (approximately 75% reduction). Figure 6J shows clear increases in both colony numbers and sizes in A172 cells after *PRMT1* overexpression, with S-F1G quantitative results showing increases from 78±6 in controls to 203±15 (approximately 2.9-fold increase).

Cell invasion assays showed similar trends: Figure 6K demonstrates that *PRMT1* knockdown inhibited U251 cell invasive capacity, with S-F1H quantitative results showing invading cell numbers decreasing from 165±25 in controls to 62±12. Figure 6L shows *PRMT1* overexpression promoted A172 cell ability to penetrate Matrigel membranes, with S-F1I quantitative results showing increases from 80±20 in controls to 198±29. These functional experimental results (all $p<0.01$, $n\geq3$, two-tailed t-test) consistently indicate that *PRMT1*, as an oncogene, plays important regulatory roles in malignant phenotypes of glioma cells, including proliferation, colony formation, and invasion, providing solid experimental foundations for its potential as a therapeutic target.

3.7. NO Metabolism Regulation and Functional Validation of *PRMT1* in Glioma Stem Cells

To investigate effects of the nitric oxide (NO) donor SNAP on *PRMT1* expression, we conducted Western blot analysis in GBM-P3# cell lines. Results showed that with increasing SNAP concentrations (0, 50, 100, 150 μM), *PRMT1* protein band intensity was upregulated dose-dependently (Figure 7A). Quantitative analysis confirmed this trend, with *PRMT1* relative grayscale intensity significantly increasing (0 μM ~1.0 as control, 50 μM ~1.1, 100 μM ~1.5, 150 μM ~1.45; $^{**}p<0.01$ vs. 0 μM, Figure 7B). Balancing induction efficiency and cytotoxicity considerations, we selected 100 μM as the subsequent intervention concentration to avoid non-specific effects from high doses.

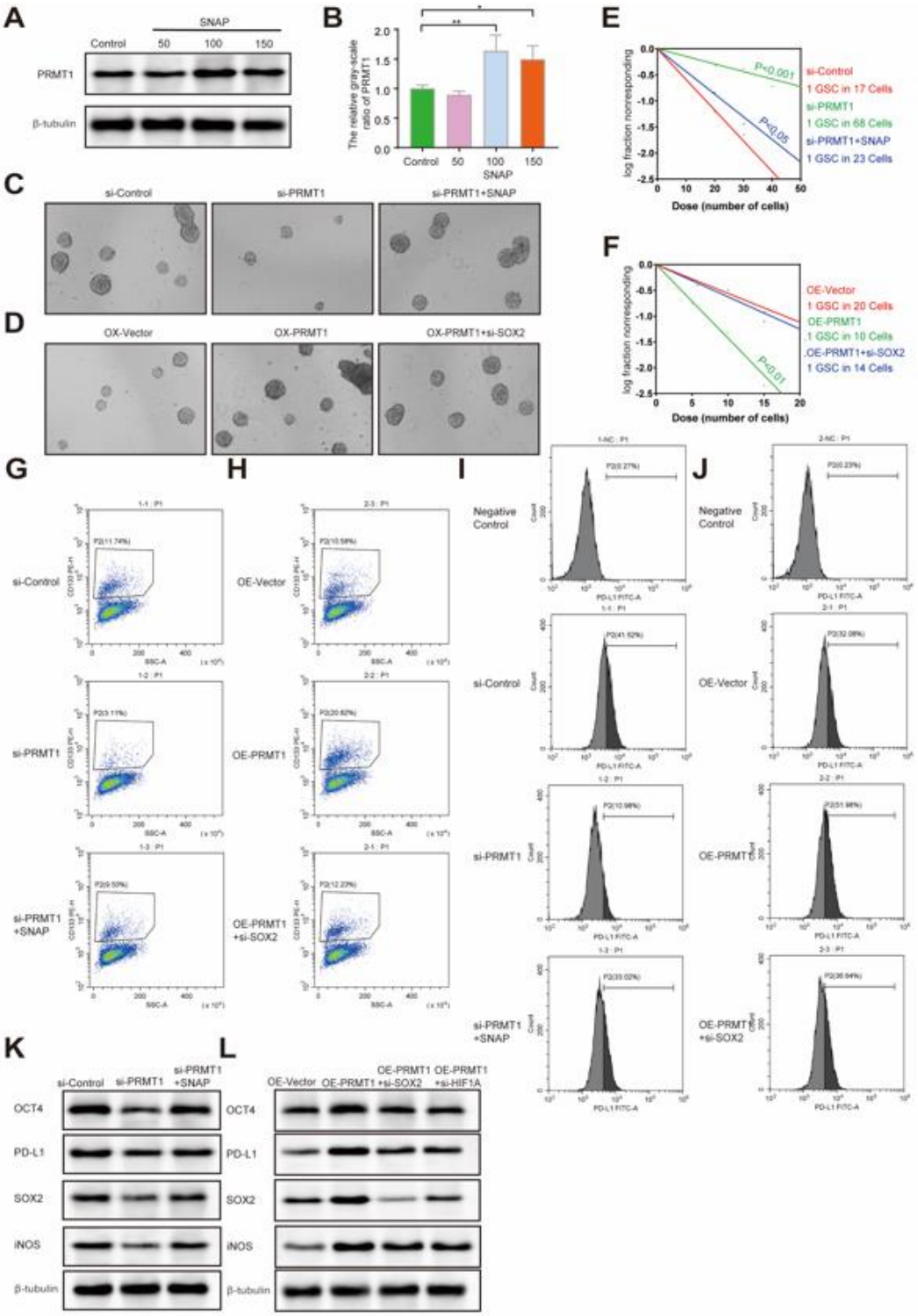

Fig. 7. NO metabolism regulation of *PRMT1* in glioma stem cells.

A) Dose-response effects of NO donor SNAP on *PRMT1* expression in GBM#P3 cells. **B)** Quantitative analysis of *PRMT1* relative expression intensity (**p<0.01 vs. 0μM). **C & D)** Stem cell sphere formation assays showing effects of *PRMT1* knockdown and overexpression. **E & F)** *In vitro* extreme limiting dilution analysis determining stem cell frequency changes. **G & J)** Flow cytometry analysis of *CD133* and *PD-L1* expression changes. **K & L)** Western blot validation of *OCT4*, *PD-L1*, *SOX2*, and *iNOS* protein expression regulation, ***p<0.001.

siRNA-mediated *PRMT1* knockdown experiments revealed changes in spheroidal morphology and numbers. si-Control group cells formed typical spheres, while si-*PRMT1* group cell spheres were significantly reduced in size and appeared looser (Figure 7C). Notably, SNAP addition (si-*PRMT1*+SNAP group, 100 μM) partially restored sphere formation, suggesting NO signaling might reverse morphological inhibition caused by *PRMT1* knockdown. Correspondingly, *PRMT1* overexpression promoted larger and more numerous GSC spheres, while co-knockdown of *SOX2* partially reversed this effect (Figure 7D).

In vitro extreme limiting dilution analysis further validated *PRMT1*'s critical role in GSC self-renewal. In GBM-P3 cell lines, non-responsive fractions in si-Control groups decreased with increasing cell dilution, corresponding to stem cell frequencies of approximately 1/17 (Figure 7E). *PRMT1* knockdown shifted curves upward, reducing stem cell frequencies to approximately 1/68, indicating inhibited self-renewal capacity. Interestingly, si-*PRMT1*+SNAP group curves partially shifted downward, restoring frequencies to about 1/23, suggesting NO signal-mediated *PRMT1* upregulation promotes stemness maintenance. Overexpression experiments showed inverse trends: compared to OE-Vector groups (frequency ~1/20), OE-*PRMT1* group stem cell frequencies increased to approximately 1/10, while combined si-*SOX2* treatment reduced frequencies to about 1/14 (Figure 7F). These data demonstrate *PRMT1* regulates GSC self-renewal and stemness maintenance through NO-dependent mechanisms.

Flow cytometry analysis evaluated *PRMT1*'s regulatory effects on key stemness markers. *CD133* expression analysis showed positive cell percentages of 11.74% in si-Control groups, significantly reduced to 3.11% after *PRMT1* knockdown, and partially restored to 9.50% by SNAP treatment (Figure 7G). In overexpression experiments, OE-*PRMT1* group *CD133* positivity rates increased from 10.58% in controls to 20.82%, decreasing to 12.23% after combined *SOX2* knockdown (Figure 7H). Similarly, *PD-L1* expression patterns showed comparable trends: in knockdown groups, positivity rates were 41.52% in si-Control groups, decreased to 10.98% in si-*PRMT1* groups, and partially recovered to 33.02% after SNAP treatment (Figure 7I). Overexpression results indicated OE-*PRMT1* group *PD-L1* positivity rates increased from 32.08% in controls to 51.98%, decreasing to 36.64% with *SOX2* co-knockdown (Figure 7J).

Western blot analysis at protein levels further validated these observations. In knockdown experiments, *OCT4*, *PD-L1*, *SOX2*, and *iNOS* expression was significantly downregulated in si-*PRMT1* groups, with band intensities reduced by 60-80% (Figure 7K). SNAP treatment partially restored these protein levels, with recovery amplitudes of 20-48%. Supplementary Figures S-F-2A-D densitometric analysis confirmed these trends. Overexpression experiments revealed inverse regulatory patterns: OE-*PRMT1* groups showed upregulation of these proteins by 0.36-1.1 fold, while combined knockdown of *SOX2* or HIF1A resulted in partial downregulation (Figure 7L). Quantitative analysis indicated relative expression of each protein in OE-*PRMT1* groups was 1.3-2.13 times controls (***$p<0.001$ vs. OE-Vector, S-F-2E-H). These results unveil multifaceted functional networks of *PRMT1* under NO metabolic regulation, not only maintaining GSC stemness features (*CD133*, *OCT4*, *SOX2*) but also promoting establishment of immunosuppressive environments (*PD-L1*), providing robust experimental evidence for *PRMT1* as a glioma therapeutic target.

3.8. *In Vivo* Validation of *PRMT1* Knockdown in Glioma Mouse Models and Mechanistic Modeling

To validate *PRMT1*'s function in glioma progression, we established orthotopic glioma mouse models using luciferase-labeled GL261-Luc cells stereotactically injected into mouse brains. Bioluminescence imaging results clearly demonstrated anti-tumor effects of *PRMT1* knockdown: sh-Control mice exhibited strong fluorescent signals reflecting rapid tumor growth, while sh-*PRMT1* mice showed significantly attenuated fluorescent signals, suggesting effective tumor growth inhibition (Figure 8A). Quantitative analysis confirmed these observations, with fluorescence intensity (photon flux) in sh-*PRMT1* groups decreasing to approximately 35% of sh-Control groups (***$p<0.001$), definitively demonstrating significant anti-tumor effects of *PRMT1* knockdown (Figure 8B).

H&E staining further validated tumor volume and invasiveness differences from histomorphological perspectives. Brain sections showed large tumor areas with indistinct borders, accompanied by evident cellular proliferation, increased nuclear mitotic figures, and neovascularization in sh-Control groups (Figure 8C). In contrast, sh-*PRMT1* groups displayed significantly smaller tumor regions, notably reduced cell density, attenuated invasive borders, and relatively increased necrotic areas. These histological changes were highly consistent with bioluminescence imaging results, morphologically confirming inhibitory effects of *PRMT1* knockdown on glioma expansion *in vivo*.

SOX2, a critical tumor stemness marker, exhibited high nuclear expression in sh-Control tumor tissues, with positive cells widely distributed throughout tumor parenchyma (Figure 8D). Following *PRMT1* knockdown, *SOX2*-positive cell numbers significantly decreased, staining intensity noticeably attenuated, and distribution concentrated primarily at tumor margins. Similarly, *PD-L1*, a key immunosuppression molecule, was widely expressed on tumor cell membranes and cytoplasm in sh-Control groups, presenting diffuse distribution patterns (Figure 8E). sh-*PRMT1* groups showed markedly downregulated *PD-L1* expression levels and substantially decreased positive cell proportions. These results indicate *PRMT1* knockdown not only inhibited tumor stemness maintenance but also effectively ameliorated tumor-induced immunosuppressive microenvironments.

4. Conclusion

This study systematically elucidated *PRMT1*'s critical role in glioma progression and its regulatory relationship with nitric oxide metabolism through integrated multi-omics data analysis, *in vitro* functional validation, and *in vivo* model confirmation. Based on comprehensive experimental evidence, our constructed *PRMT1* bidirectional regulatory mechanism model (Figure 8F) demonstrates: under high *PRMT1* expression (left model), *PRMT1* epigenetically upregulates stemness

transcription factors like *OCT4* and *SOX2*, maintaining glioblastoma stem cell self-renewal capacity. Simultaneously, it activates *iNOS* expression to promote nitric oxide synthesis and significantly upregulates *PD-L1* expression to establish immunosuppressive barriers, driving tumor-associated macrophage polarization toward M2 phenotypes and affecting surrounding astrocyte and neuronal functions.

Conversely, *PRMT1* knockdown (right model) disrupts this regulatory network: *OCT4*, *SOX2*, and *iNOS* expression are significantly downregulated, disrupting GSC stemness maintenance programs; *PD-L1* expression decreases, reactivating immune surveillance functions; functional experiments show stem cell frequencies dropping from 1/17 to 1/68, *CD133* positive cell proportions decreasing from 11.74% to 3.11%; *in vivo* validation shows *PRMT1* knockdown reduces tumor fluorescence intensity in mouse brains to 35% of controls, with significantly diminished tumor volumes. These results highlight *PRMT1* as a core node connecting tumor stemness maintenance and immune evasion, whose targeted knockdown can simultaneously attack tumor stem cell populations and reshape immunosuppressive microenvironments, providing new targets for precision glioma therapy.

5. Discussion

Through multi-omics data integration and functional validation, this study elucidated *PRMT1*'s critical role in glioma progression, particularly its regulatory relationship with nitric oxide metabolism and central position in maintaining tumor stemness and promoting immune evasion. These findings not only deepen understanding of malignant biological characteristics of gliomas but also offer novel insights for developing precision therapeutic strategies.

Microdissected sequencing analysis based on the IVY Glioblastoma database revealed significant spatial heterogeneity of *PRMT1* and *NOS2* across different glioma histological regions [28, 29]. This discovery underscores the unique value of spatial transcriptomics in dissecting gene-function relationships. Traditional bulk RNA sequencing, unable to differentiate contributions from distinct cell types and spatial locations, often obscures intricate spatial expression patterns, leading to oversimplified understanding of inter-gene relationships. IVY-GAP data, utilizing laser microdissection, precisely separated different glioma histological regions, revealing *PRMT1*'s primary enrichment in high-cell-density tumor core regions, suggesting its main involvement in tumor cell proliferation and metabolic regulation [13, 30]. In contrast, high *NOS2* expression in microvascular proliferation areas is more associated with angiogenesis and inflammatory microenvironment regulation.

This complementary spatial distribution further supports synergistic mechanisms between the two in glioma progression. Just as single-cell RNA sequencing in this study identified NO metabolism-related cell subpopulations and functional states uncapturable by bulk sequencing, spatial transcriptomics provides another crucial dimension for understanding gene expression complexity.

This study confirms significant advantages of *PRMT1* as a glioma therapeutic target. Its high expression in gliomas is closely linked to poor patient prognosis, validated across multiple independent cohorts, demonstrating robust biomarker characteristics [29, 30]. To enhance result robustness, we conducted supplementary analyses using external validation datasets like GlioVis, showing high consistency in *PRMT1* expression patterns and prognostic relevance across different cohorts, further supporting its reliability as an independent prognostic factor (31). *PRMT1*'s dual regulatory mechanism makes it an ideal therapeutic target, capable of directly attacking tumor stem cell populations while simultaneously reshaping immunosuppressive microenvironments. Both *in vitro* and *in vivo* experiments confirmed *PRMT1* knockdown significantly inhibits tumor growth, reduces stem cell frequencies, and activates immune responses. Our *in vivo* validation used immunocompetent C57BL/6 mouse orthotopic transplant models, which retain intact immune systems, better simulating human glioma tumor microenvironments and enhancing accuracy of *PRMT1* immunomodulatory function assessments.

However, *PRMT1*, as an epigenetic regulatory enzyme, also plays vital roles in normal cells. Achieving tumor-specific targeting represents a key challenge for future research. Additionally, differences in *PRMT1* expression patterns among various glioma molecular subtypes suggest potential needs for individualized treatment strategies [13, 14, 29, 30].

This study uncovers the dualistic role of NO metabolism in glioma progression: high NO metabolism levels positively correlate with tumor malignancy, promoting stemness maintenance and immunosuppression through *PRMT1* activation, while moderate NO signaling may participate in normal cellular metabolism and immune regulation. This complexity reflects NO's multifaceted biological functions within tumor microenvironments, including angiogenesis, inflammation regulation, apoptosis, and metabolic reprogramming. Therefore, NO metabolism-based therapeutic strategies require precise dosage and timing control to avoid adverse effects from excessive inhibition.

This research successfully integrated multiple omics technologies, including bulk RNA sequencing, single-cell sequencing, and spatial transcriptomics, providing technical paradigms for comprehensively unraveling glioma heterogeneity. Particularly, single-cell sequencing applications enabled us to identify associations between NO metabolism and tumor stemness previously masked in bulk sequencing, while spatial transcriptomics further revealed spatial patterns of gene expression, offering new perspectives for understanding complex tumor microenvironments.

Despite achieving significant findings, this study has limitations warranting improvement in future research. Although we employed C57BL/6 mouse orthotopic tumor models for validation, tumor growth dynamics in these models may differ from human gliomas due to species differences. Future studies could consider using patient-derived xenograft models to further bridge clinical relevance. This study primarily relied on retrospective data analysis and in vitro experiments, lacking prospective clinical validation. *PRMT1*'s safety and efficacy as a therapeutic target require further evaluation in clinical trials. While we

identified associations between *PRMT1* and NO metabolism, specific molecular mechanisms require more in-depth research for elucidation. Concurrently, molecular features of gliomas may vary among different populations, and the universality of findings in this study across other populations requires further validation, despite preliminary support from external datasets like GlioVis.

Based on these findings, future research can proceed in multiple directions including mechanistic studies, therapeutic strategies, and clinical translation. At mechanistic levels, further elucidation of specific molecular mechanisms by which *PRMT1* regulates NO metabolism is needed, including its interactions with key transcription factors and signaling pathways. Regarding therapeutic strategies, *PRMT1*-specific inhibitors can be developed, or their combined applications with immune checkpoint inhibitors, radiotherapy, or chemotherapy can be explored. For clinical translation, patient stratification systems based on *PRMT1* expression need establishment to guide individualized treatments. Integrating multimodal spatial omics technology development holds promise for comprehensively elucidating NO metabolism regulatory networks in complex glioma microenvironments, providing more refined molecular maps for precision medicine implementation.

In summary, this study not only reveals *PRMT1*'s critical role in glioma progression but also provides new targets and strategies for precision glioma therapy. With ongoing technological advancements and deeper research, *PRMT1* is poised to become a significant breakthrough in glioma treatment, contributing importantly to improving patient prognosis.

Conflicts of Interest

None.

Funding

This work was supported by the Doctoral Youth Foundation, The Affiliated Yantai Yuhuangding Hospital of Qingdao University (YHDYY-2022012), and the Natural Science Foundation of Shandong Province (ZR2023MH245). The funding bodies had no role in the design of the study, data collection, analysis, interpretation, or manuscript writing.

Ethical Approval

Ethical approval for this study was obtained from the Research Ethics Committee of Yantaishan Hospital. The approval reference number is YTM-2025193. All procedures involving human participants were conducted in accordance with the ethical standards of the institutional and national research committee and the 1964 Helsinki Declaration and its later amendments.

Author Contributions

KX conceived the study and, together with YK, designed the experiments. JYC and YG performed bioinformatics analyses. KX and ST conducted the animal experiments. CFM was responsible for statistical analysis and figure preparation. Pathological analysis was performed by JYC. YK and JYC drafted the manuscript. XHT and HYW contributed substantially to manuscript revision. All authors read and approved the final manuscript.

Guarantor

Dr. Yang Kong takes full responsibility for the integrity of the work, the accuracy of the data, and the decision to submit the manuscript for publication.

References

[1] Mackenzie Price, Christine Ballard, Julia Benedetti, et al. “CBTRUS Statistical Report: Primary Brain and Other Central Nervous System Tumors Diagnosed in the United States in 2017–2021.” *Neuro Oncol*, vol. 26, no. Supplement_6, pp. vi1-vi85, 2024. View at: Publisher Site | PubMed

[2] Lauren R Schaff, Ingo K Mellinghoff “Glioblastoma and Other Primary Brain Malignancies in Adults: A Review.” *JAMA*, vol. 329, no. 7, pp. 574-587, 2023. View at: Publisher Site | PubMed

[3] Ainhoa Hernández, Marta Domènech, Ana M Muñoz-Mármol, et al. “Glioblastoma: Relationship between Metabolism and Immunosuppressive Microenvironment.” *Cells*, vol. 10, no. 12, pp. 3529, 2021. View at: Publisher Site | PubMed

[4] Yang Liu, Heba Ali, Fatima Khan, et al. “Epigenetic regulation of tumor-immune symbiosis in glioma.” *Trends Mol Med*, vol. 30, no. 5, pp. 429-442, 2024. View at: Publisher Site | PubMed

[5] Abhishek D Garg, Dominika Nowis, Jakub Golab, et al. “Immunogenic cell death, DAMPs and anticancer immunity.” *Biochim Biophys Acta*, vol. 1805, no. 1, pp. 53-71, 2010. View at: Publisher Site | PubMed

[6] Jade D Bailey, Marina Diotallevi, Thomas Nicol, et al. “Nitric Oxide Modulates Metabolic Remodeling in Inflammatory Macrophages through TCA Cycle Regulation and Itaconate Accumulation.” *Cell Rep*, vol. 28, no. 1, pp. 218-230.e7, 2019. View at: Publisher Site | PubMed

[7] Federica Vannini, Khosrow Kashfi, Niharika Nath “The dual role of iNOS in cancer.” *Redox Biol*, vol. 6, pp. 334-343, 2015. View at: Publisher Site | PubMed

[8] Anh N Tran, Nathaniel H Boyd, Kiera Walker, et al. “NOS Expression and NO Function in Glioma and Implications for Patient Therapies.” *Antioxid Redox Signal*, vol. 26, no. 17, pp. 986-999, 2017. View at: Publisher Site | PubMed

[9] Tammy Linlin Song, Maarja-Liisa Nairismägi, Yurike Laurensia, et al. “Oncogenic activation of the STAT3 pathway drives PD-L1 expression in natural killer/T-cell lymphoma.” *Blood*, vol. 132, no. 11, pp. 1146-1158, 2018. View at: Publisher Site | PubMed

[10] Muhammad Zaeem Noman, Giacomo Desantis, Bassam Janji, et al. “PD-L1 is a novel direct target of HIF-1α, and its blockade under hypoxia enhanced MDSC-mediated T cell activation.” *J Exp Med*, vol. 211, no. 5, pp. 781-790, 2014. View at: Publisher Site | PubMed

[11] K B Sandau, J Fandrey, B Brüne "Accumulation of HIF-1α under the influence of nitric oxide." *Blood*, vol. 97, no. 4, 1009-1015, 2001. View at: Publisher Site | PubMed

[12] Charlène Thiebaut, Louisane Eve, Coralie Poulard, et al. "Structure, Activity, and Function of PRMT1." *Life (Basel)*, vol. 11, no. 11, pp. 1147, 2021. View at: Publisher Site | PubMed

[13] Shiquan Shen, Honglong Zhou, Zongyu Xiao, et al. "PRMT1 in human neoplasm: cancer biology and potential therapeutic target." *Cell Communication and Signaling*, vol. 22, no. 1, pp. 102, 2024. View at: Publisher Site

[14] Jing Liu, Xia Bu, Chen Chu, et al. "PRMT1 mediated methylation of cGAS suppresses anti-tumor immunity." *Nat Commun*, vol. 14, no. 1, pp. 2806, 2023. View at: Publisher Site | PubMed

[15] Laura M Richards, Owen K N Whitley, Graham MacLeod, et al. "Gradient of Developmental and Injury Response transcriptional states defines functional vulnerabilities underpinning glioblastoma heterogeneity." *Nat Cancer*, vol. 2, no. 2, pp. 157-173, 2021. View at: Publisher Site | PubMed

[16] Zheng Zhao, Ke-Nan Zhang, Qiangwei Wang, et al. "Chinese Glioma Genome Atlas (CGGA): A Comprehensive Resource with Functional Genomic Data from Chinese Glioma Patients." *Genomics Proteomics Bioinformatics*, vol. 19, no. 1, pp. 1-12, 2021. View at: Publisher Site | PubMed

[17] Michele Ceccarelli, Floris P Barthel, Tathiane M Malta, "Discrete Subsets and Pathways of Progression in Diffuse Glioma." *Cell*, vol. 164, no. 3, pp. 550-563, 2016. View at: Publisher Site | PubMed

[18] Ralph B Puchalski, Nameeta Shah, Jeremy Miller, et al. "An anatomic transcriptional atlas of human glioblastoma." *Science*, vol. 360, no. 6389, pp. 660-663, 2018. View at: Publisher Site | PubMed

[19] Cole Trapnell, Davide Cacchiarelli, Jonna Grimsby, et al. "The dynamics and regulators of cell fate decisions are revealed by pseudotemporal ordering of single cells." *Nat Biotechnol*, vol. 32, no. 4, pp. 381-386, 2014. View at: Publisher Site | PubMed

[20] Yuhan Hao, Tim Stuart, Madeline H Kowalski, et al. "Dictionary learning for integrative, multimodal and scalable single-cell analysis." *Nat Biotechnol*, vol. 42, no. 2, pp. 293-304, 2024. View at: Publisher Site | PubMed

[21] Minoru Kanehisa, Miho Furumichi, Yoko Sato, et al. "KEGG: biological systems database as a model of the real world." *Nucleic Acids Res*, vol. 53, no. D1, pp. D672-D677, 2025. View at: Publisher Site

[22] M Ashburner, C A Ball, J A Blake, et al. "Gene ontology: tool for the unification of biology. The Gene Ontology Consortium." *Nat Genet*, vol. 25, no. 1, pp. 25-29, 2000. View at: Publisher Site | PubMed

[23] Arthur Liberzon, Aravind Subramanian, Reid Pinchback, et al. "Molecular signatures database (MSigDB) 3.0." *Bioinformatics*, vol. 27, no. 12, pp. 1739-1740, 2011. View at: Publisher Site | PubMed

[24] Aravind Subramanian, Pablo Tamayo, Vamsi K Mootha, et al. "Gene set enrichment analysis: a knowledge-based approach for interpreting genome-wide expression profiles." *Proc Natl Acad Sci U S A*, vol. 102, no. 43, pp. 15545-15550, 2005. View at: Publisher Site | PubMed

[25] Aaron M Newman, Chloé B Steen, Chih Long Liu, et al. "Determining cell type abundance and expression from bulk tissues with digital cytometry." *Nat Biotechnol*, vol. 37, no. 7, pp. 773-782, 2019. View at: Publisher Site | PubMed

[26] Ryan J. Tibshirani "The lasso problem and uniqueness." *Electron J Statist*, vol. 7, pp. 1456-1490, 2013. View at: Publisher Site

[27] Yifang Hu, Gordon K Smyth "ELDA: extreme limiting dilution analysis for comparing depleted and enriched populations in stem cell and other assays." *J Immunol Methods*, vol. 347, no. 1-2, pp. 70-78, 2009. View at: Publisher Site | PubMed

[28] Paola Palumbo, Francesca Lombardi, Giuseppe Siragusa, et al. "Involvement of NOS2 Activity on Human Glioma Cell Growth, Clonogenic Potential, and Neurosphere Generation." *Int J Mol Sci*, vol. 19, no. 9, pp. 2801, 2018. View at: Publisher Site | PubMed

[29] Hong Li, Xiaoyan Qi, Lijun He, et al. "PRMT1 promotes radiotherapy resistance in glioma stem cells by inhibiting ferroptosis." *Jpn J Radiol*, vol. 43, no. 1, pp. 129-137, 2025. View at: Publisher Site | PubMed

[30] Yike Chen, Xiaohui Xu, Kaikai Ding, et al. "TRIM25 promotes glioblastoma cell growth and invasion via regulation of the PRMT1/c-MYC pathway by targeting the splicing factor NONO." *Journal of Experimental & Clinical Cancer Research*, vol. 43, no. 1, pp. 39, 2024. View at: Publisher Site